

uncertainties of the obtained source parameters. To illustrate, we have taken the Mw 5.4 Ridgecrest earthquake on July 6, 2019, as an example (event ID 38450263, 35.76033°/-117.57500°/7.0 km, 2019/07/05 11:07:53.04). Our analysis reveal that this earthquake consisted of two subevents (E1 and E2). The second of these subevents (E2) likely ruptured 1.3 km along the strike and 1.0 km along the dip directions (Meng and Fan, 2021). We first perform empirical Green's function (eGf) analysis on the Mw 5.4 earthquake. We obtain the apparent source time functions (ASTFs) at each individual station. This is achieved by deconvolving seismograms of the Mw 5.4 event with those of a nearby M 3.7 earthquake (event ID 38448791, 35.75033°/-117.56317°/6.9 km, 2019/07/05 07:27:37.11), to remove path and site effects for both P and S waves. We use stations from regional broadband networks and strong-motion networks. The seismic records are band-pass filtered at 0.5 to 20.0 Hz with a causal 2nd-order Butterworth filter. Examination of the ASTFs shows clearly separated episodes, indicating two major subevents, E1 and E2. We estimate the seismic moments of E1 and E2 by computing an average moment ratio between the two episodes, requiring that the total moment equaled that of a Mw 5.4 earthquake. For each ASTF, we obtain a moment ratio by dividing the subevent moments, integrating the episodes respectively. The moment ratio of E1 to E2 is about 5%, equivalent to a Mw 4.5 earthquake for E1. We estimate the centroid location separation distance by curve fitting the centroid lag time at different directions (Figures 1b). The centroid location of E2 is 1.1 km northeast of E1. This suggests that the earthquake ruptured a fault plane orthogonal to the main fault strike of the Mw 7.1 mainshock (Shelly, 2020).

Using the ASTFs in conjunction with a local 1D velocity model, we determine the rupture length and width of subevent E2 by estimating its second seismic moments. This 1D velocity model is obtained by averaging the community velocity model of Southern California (Lee et al., 2014). We follow a method outlined in Meng et al. (2020) to solve the second moments of the earthquake (McGuire, 2004, 2017). The second seismic moments characterize the variances of these first moments (centroids). Effectively, they provide critical information about the earthquake's characteristics, such as its length, width, duration, and rupture directivity (Backus and Mulcahy, 1976a,b; McGuire, 2004). Knowing the local velocity structure, the second seismic moments $\hat{\mu}^{(2,0)}$, $\hat{\mu}^{(0,2)}$, and $\hat{\mu}^{(1,1)}$ can be obtained by solving:

$$\hat{\mu}^{(0,2)}(\underline{s}) = \hat{\mu}^{(0,2)} - 2\underline{s} \cdot \hat{\mu}^{(1,1)} + \underline{s} \cdot \hat{\mu}^{(2,0)} \underline{s} \quad (1)$$

where $\hat{\mu}^{(0,2)}(\underline{s})$ is the apparent duration obtained from the ASTF and \underline{s} is the slowness of either P or S waves in the source region for a given source-receiver pair (McGuire, 2004). The second moments can estimate an earthquake characteristic duration ($\tau_c = 2\sqrt{\hat{\mu}^{(0,2)}}$) and earthquake characteristic rupture extents ($x_c(\hat{n}) = 2\sqrt{\hat{n}^T \hat{\mu}^{(2,0)} \hat{n}$), where \hat{n} is a unit eigenvector of $\hat{\mu}^{(2,0)}$ and x_c represents the associated rupture dimension, e.g., the rupture length L_c or the rupture width W_c (McGuire, 2004).

We further compute the strain-tensor perturbations on the fault plane generated by E1 by calculating the numerical spatial derivatives of the displacement field. We then use Hooke's law to obtain the stress perturbations. The subevent E2 is situated in a region where both static and dynamic stress perturbations from the immediate foreshock exceed 0.1 MPa (Figure 1b), promoting an instantaneous slip event in the area. Our source model shows an evolving rupture process in which the immediate foreshock cascades to nucleate the sequential stage rupture, E2, through a stress-triggering process. This confirms our interpretation that E1 is causally related to E2. Additionally, we identify similar immediate foreshocks in 527 events, spanning a broad magnitude range of $0.9 \leq M \leq 5.4$. These immediate foreshocks are adjacent to the mainshocks and precede them by less than 100 seconds, suggesting causal triggering relations. However, the attributes of the immediate foreshocks do not appear to scale with the mainshock magnitude. These observations imply that earthquake rupture may initiate in a universal manner but evolves stochastically. Our findings indicate that the development of earthquake rupture is likely controlled by fine-scale fault heterogeneities, and the final magnitude is the only distinguishing factor between small and large earthquakes. Our results highlight the importance of resolving finite-source attributes of small earthquakes.

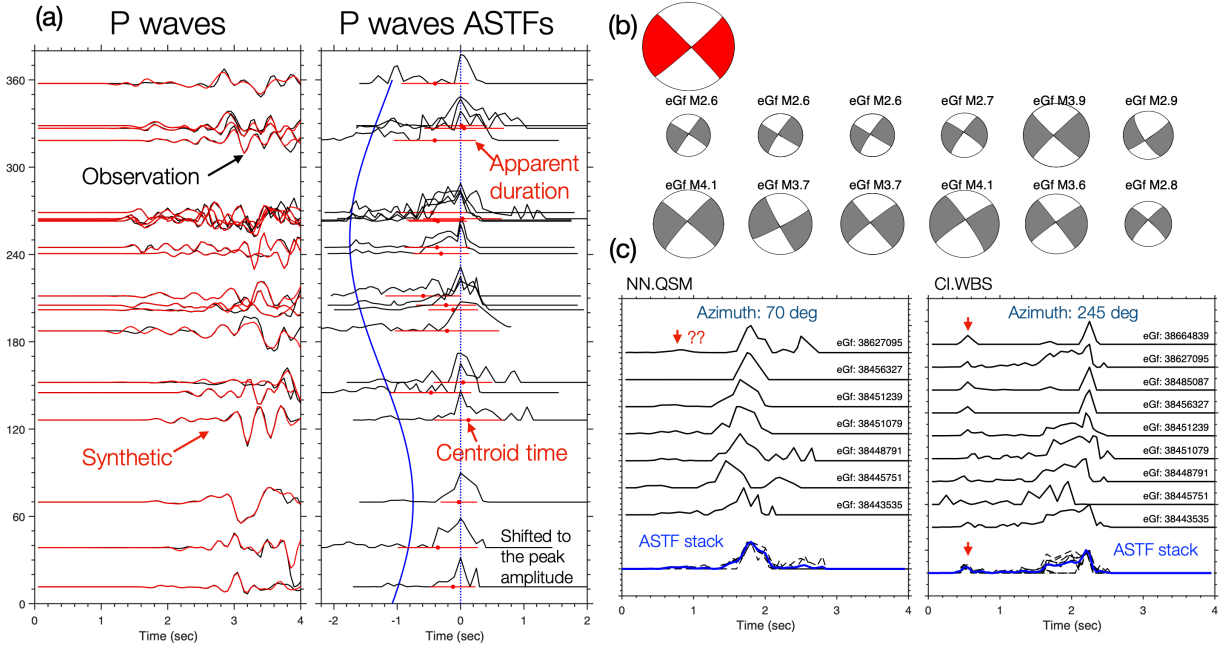


Figure 2: Example of obtaining the apparent source time function (ASTF) using eGf deconvolution analysis. (a) Observed and synthetic P waves, along with their associated ASTFs. (b) Focal mechanism of the main-shock (Mw 5.4 example earthquake) and available eGfs. (c) Example ASTFs of two stations, representing the forward and backward rupture directions.

In the example of the Mw 5.4 Ridgecrest earthquake, apparent source time functions (ASTFs) can offer significant insights into the earthquake rupture kinematics. However, it is worth noting that ASTFs are typically obtained through eGf deconvolution, a technique that might not consistently yield robust results. The reliability of the ASTFs has a direct influence on the inferred second moments, making the analysis of potential uncertainties crucial. During the project, we have investigated the uncertainties that may associate with conventional eGf deconvolution methods (Fan et al., 2022). In contrast to conventional frequency-domain deconvolution methods, we obtain the ASTFs by performing eGf deconvolution in the time domain. This approach constructs the deconvolution as a linear inverse problem with a non-negativity constraint (Fan and McGuire, 2018). We perform eGf deconvolution for all target events shown in Figure 1a. Specifically, we set the P-wave window length to range from -1 to 4 seconds and the S-wave window length to range from -1 to 5 seconds, relative to the predicted arrival times. The eGf phase windows are set at -1 to 1.5 seconds for P waves and -1 to 2 seconds for S waves, respectively.

Different eGfs can be used to obtain ASTFs separately, and we construct an average ASTF for each station by stacking the ASTFs from qualified eGfs. In the example case, there are 12 eGfs located within 3 km of the event, both horizontally and in depth. We require that the correlation values between the target earthquake and eGf moment tensors be greater than 0.9. As shown in Figure 2, the ASTFs of the Mw 5.4 Ridgecrest earthquake prove to be complex. Beyond the two major subevents, E1 and E2, a multitude of subevents may have taken place during E2 (Figure 2b). The ASTFs obtained vary when employing different eGfs (Figure 2c), even though all of them can generate synthetic seismograms that fit the observations equally well. These variations in the ASTFs for the same earthquake at the same station underscore the uncertainties in the ASTFs. Considering that the ASTFs can explain the observations using their respective eGfs, the findings imply a need for further quantification or the development of novel methods to enhance

the robustness of the apparent source time functions.

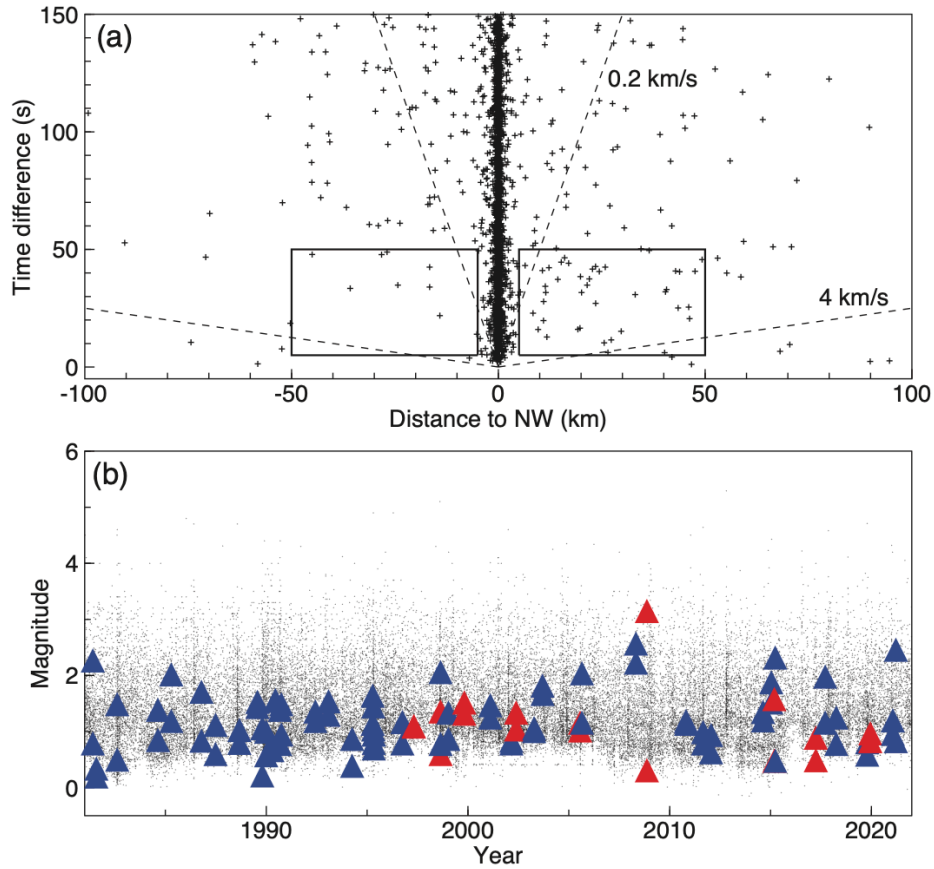


Figure 3: (a) Time and distance offsets for closely spaced earthquake pairs in our central San Andreas Fault (CSAF) study region. Each point shows the delay time and horizontal distance offset of the second event relative to the first event. The diagonal lines show reference velocities of 0.2 and 4 km/s. The rectangles show the 5 to 50 s and 5 to 50 km window where the along-fault asymmetry appears especially strong. (b) Magnitude versus time for earthquakes in our CSAF study region. The red and blue triangles show the near-contemporaneous earthquake pairs inside the boxes plotted in panel (a), with red for southeastward offsets and blue for northwestward offsets.

Lastly, we use seismicity to infer fault-slip behaviors in the central San Andreas Fault (Shearer and Fan, 2023). For more than 40 years, the San Andreas Fault in California, stretching between Parkfield and San Juan Bautista, has been subject to surface fault creep as well as numerous small earthquakes at depth. In our research, we seek pairs of these earthquakes that are separated temporally by 5 to 50 seconds and spatially by 5 to 50 kilometers (Figure 3). Among the 51 pairs that have occurred since 1981, the second (subsequent) event is typically located to the northwest of the first. This spatial asymmetry is challenging to reconcile with existing earthquake triggering models, suggesting the presence of an underlying process that connects these events across substantial distances.

References

- Backus, G. and M. Mulcahy, 1976a: Moment tensors and other phenomenological descriptions of seismic sources-i. continuous displacements. *Geophysical Journal International*, **46** (2), 341–361.
- Backus, G. and M. Mulcahy, 1976b: Moment tensors and other phenomenological descriptions of seismic sources-ii. discontinuous displacements. *Geophysical Journal International*, **47** (2), 301–329.
- Fan, W. and J. J. McGuire, 2018: Investigating microearthquake finite source attributes with iris community wavefield demonstration experiment in oklahoma. *Geophysical Journal International*, **214** (2), 1072–1087.
- Fan, W., H. Meng, D. T. Trugman, J. J. McGuire, and E. S. Cochran, 2022: Finite-source attributes of m4 to 5.5 ridgecrest, california earthquakes. *AGU Fall Meeting Abstracts*, Vol. 2022, S15C–0209.
- Lee, E.-J., P. Chen, T. H. Jordan, P. B. Maechling, M. A. Denolle, and G. C. Beroza, 2014: Full-3-D tomography for crustal structure in southern California based on the scattering-integral and the adjoint-wavefield methods. *Journal of Geophysical Research: Solid Earth*, **119** (8), 6421–6451.
- McGuire, J. J., 2004: Estimating finite source properties of small earthquake ruptures. *Bulletin of the Seismological Society of America*, **94** (2), 377–393, doi:10.1785/0120030091.
- McGuire, J. J., 2017: A MATLAB toolbox for estimating the second moments of earthquake ruptures. *Seismological Research Letters*, **88** (2A), 371–378, doi:10.1785/0220160170.
- Meng, H. and W. Fan, 2021: Immediate foreshocks indicating cascading rupture developments for 527 m 0.9 to 5.4 ridgecrest earthquakes. *Geophysical Research Letters*, **48** (19), e2021GL095 704.
- Meng, H., J. J. McGuire, and Y. Ben-Zion, 2020: Semiautomated estimates of directivity and related source properties of small to moderate southern california earthquakes using second seismic moments. *Journal of Geophysical Research: Solid Earth*, **125** (4), e2019JB018 566.
- Shearer, P. M. and W. Fan, 2023: Space–time asymmetry in earthquake pairs along the central san andreas fault: Evidence for small earthquake links at long distances. *The Seismic Record*, **3** (2), 77–85.
- Shelly, D. R., 2020: A high-resolution seismic catalog for the initial 2019 ridgecrest earthquake sequence: Foreshocks, aftershocks, and faulting complexity. *Seismological Research Letters*, **91** (4), 1971–1978.